Article

Not peer-reviewed version

Non-axisymmetric Bouncing Dynamics on a Moving Superhydrophobic Surface

Wenhao Wang , Wenlong Yu , Zhiyuan Yu , Shuo Chen , Damin Cao , Xiaohua Liu , Jiayi Zhao *

Posted Date: 28 November 2023

doi: 10.20944/preprints202311.1790.v1

Keywords: superhydrophobic substrate; droplet impact; spreading dynamics; contact time

Article

Non-Axisymmetric Bouncing Dynamics on a Moving Superhydrophobic Surface

Wenhao Wang [1], Wenlong Yu [1], Zhiyuan Yu [2], Shuo Chen [2], Damin Cao [3], Xiaohua Liu [4,5] and Jiayi Zhao [1,*]

[1] School of Energy and Power Engineering, University of Shanghai for Science and Technology, Shanghai, 200093, China
[2] School of Aerospace Engineering and Applied Mechanics, Tongji University, Shanghai 200092, China
[3] School of Air Transportation, Shanghai University of Engineering Science, Shanghai 201620, China
[4] School of Aeronautics and Astronautics, Shanghai Jiao Tong University, Shanghai 200030, China
[5] Key Laboratory (Fluid Machinery and Engineering Research Base) of Sichuan Province, Xihua University, Chengdu 610000, China
* Correspondence: karl_jiayi@usst.edu.cn

Abstract: The phenomenon of droplet impact on moving surfaces is widely observed in fields such as transportation, rotating machinery, and inkjet printing. Droplets exhibit non-axisymmetric behavior due to the motion of solid surfaces which significantly determines core parameters such as contact time, maximum spreading radius, and bounding velocity, thereby affecting the efficiency of related applications. In this study, we focus on kinetics and morphology of the non-axisymmetric bouncing behaviors for droplets impacting on a moving superhydrophobic surface (SHPS) within the normal (We_n) and tangential (We_t) Weber numbers. Considering the influences of moving surface on the contact area and contact time, the previous scaling formula for the horizontal velocity of droplets has been improved. Based on the velocity superposition hypothesis, we establish a theoretical model for the ratio of the maximum spreading radius at both ends depending on We_n and We_t. This research provides both experimental and theoretical evidence for understanding and controlling the non-axisymmetric behavior of droplets impacting on moving surfaces.

Keywords: uperhydrophobic substrate; droplet impact; spreading dynamics; contact time

I. Introduction

During the process of liquid droplet impact, various phenomena such as stacking, rebounding, and splashing can occur under the influence of the droplet properties and surface characteristics [1-3]. The rebound process refers to the lateral spreading of the droplet, with the conversion of kinetic energy to surface energy, gradually reaching the maximum spreading length D_{max}, after which the droplet recoils towards the center until it reaches a certain degree of contraction. Subsequently, the droplet rebounds from the surface [4-6]. The phenomenon of droplet impact has been extensively studied both numerically and experimentally [7,8], the rebound behavior of liquid droplets is influenced by various factors such as droplet properties [9,10], droplet radius and velocity [11,12], surface properties [13,14], and incident angle [15,16].

In previous studies on droplet impact, the predominant focus on stationary surfaces, and the maximum spreading length of the impacting droplet was dependent on the normal Weber number We_n, especially in cases involving low viscosity and limited wetting ability [17]. The contact time was found to be contingent upon the radius and independent of the impact velocity [18]. In this context, contact time is defined as the duration from the first contact of the droplet with the surface to the complete detachment. Research into contact time has garnered practical applications in the field of self-cleaning surfaces [19]. Here, the design of macro-textures and microstructures can effectively reduce the contact time [20,21].

However, in practical applications, droplet impact phenomena mostly occur on moving surfaces, such as raindrops impacting aircraft wings and wind turbine blades [22], and the directional transport of droplets in inkjet printing [23]. A few studies have found that on the SHPSs, as the speed of the moving surface increases, elevated surface velocities amplify the extension of impacting droplets, consequently leading to a reduction in contact time [24,25]. Similar findings have also been observed on moving surfaces with macroscopic structures and wetting patterns [26].

These conclusions mostly analyze droplets from a kinematic perspective, focusing on droplet spreading and contact time. There are still some conclusions related to momentum, some studies suggest the main cause of momentum transfer is the aerodynamic Leidenfrost effect [27]. This phenomenon refers to the thin air film formed between the droplet and the moving surface, which is the primary factor generating viscous forces on the droplet. By analyzing the forces acting on the thin air film between droplet and surface, scaling relationships can be derived to summarize the contact time, spreading ratio, and horizontal distance. These dynamic conclusions have been well validated [28]. However, in this experiments, the presence of an air film between the liquid droplet and the surface was not distinctly observe. Droplets will inevitably come into contact with the surface, and the reason for this difference may be due to insufficient surface velocity to generate a noticeable air layer. We tend to the view of the transfer of horizontal momentum is caused by the viscous boundary layer developing in the liquid [29]. Throughout the impact process, energy dissipation due to viscous losses is observed. The fundamental physical principle of non-axisymmetric bouncing dynamics is the transfer of horizontal momentum during the impact process, gradually shifting from the bottom to the top of the droplet. Based on this, formulas related to the horizontal velocity of droplets have been proposed [30], while the feasibility of this velocity formula has been well validated, there are still some sections for improvement. For example, in the derivation of this formula, the spreading region of the droplet is considered to be circular, which is accurate when impacting a stationary surface but imprecise on a moving surface, where the spreading region is elongated [28,31]. Furthermore, the contact time of the droplet is also assumed to be the same as the contact time on a stationary surface τ_s, whereas on a moving surface the contact time τ_m is shorter than τ_s [24,25].

And there is still a lack of satisfactory solutions regarding how the spreading range of droplets is influenced by surface motion. In this study, the fundamental dynamic behaviors of droplet impact on moving surfaces are focused on being revealed, a more accurate correction has been made to the scaling formula for the droplet horizontal velocity. As well as analyzing the asymmetric evolution of the spreading radius at both ends of the droplet over time caused by surface motion.

II. Methodology

We conducted experimental studies on SHPSs with horizontal movement speeds of V_t = 0-2.2m/s (corresponding to We_t = 0-116.08) using water droplets with impact velocities of V_n = 0.48-1.70m/s (corresponding to We_n = 5.69-71.26), where $\mathrm{We}_t = \rho V_t^2 D_0/\gamma$ and $\mathrm{We}_n = \rho V_n^2 D_0/\gamma$ are defined as the normal and tangential Weber number, respectively. water density $\rho \approx 1000$ kg/m^3, surface tension coefficient $\gamma \approx 0.073$ N/m, and $D_0 = 1.8 \pm 0.1$ mm was the initial diameter of the water droplets. Figure 1(a) shows the schematic diagram of the experimental apparatus, where the copper plate was polished, ultrasonically cleaned, and coated with an organic reagent three times. After drying at room temperature for 30 minutes, a solution mainly composed of nano-silica particles and silicone resin was sprayed, and the static contact angle of water droplets on the surface was about 160°(Figure 1(a)). The surface was fixed to a rotating motor to obtain the horizontal speed, and the water droplets were pushed by the injection pump (LSP01-3A) and dropped onto the SHPS under the action of gravity after separating from the needle tip. The impact velocity of the droplets was adjusted by varying the distance between the needle tip and the surface. The position of the high-speed camera (GX-8E, NAC), the point of droplet impact, and the center point of the circular hydrophobic surface are all located on the same straight line, as shown in Figure 1(b) (top view). For this experiment, the centrifugal force of the droplet on the disk can be neglected [32], therefore, the motion of the surface during droplet impact can be considered as rectilinear. The environmental temperature was about 25°C, and the humidity was around 30%.

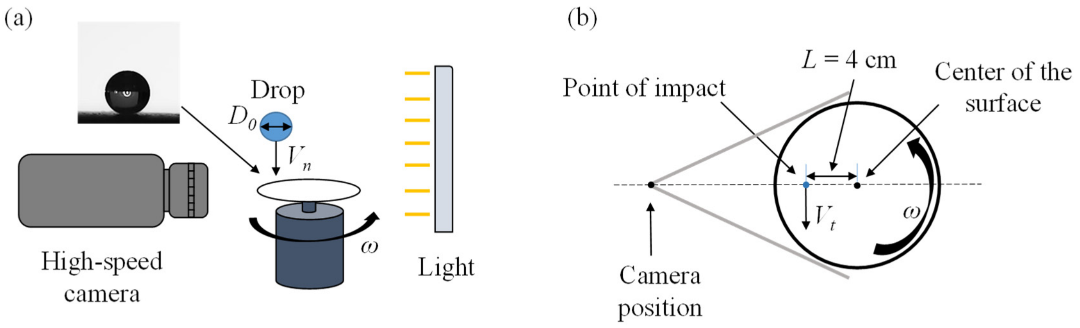

Figure 1. (a) Schematic of the experimental setup. (b) View from above showing the position of the camera, droplet impact point, and center of the circular SHPS.

III. Results and discussion

Figure 2 shows the spreading and receding stages of water droplets on a SHPS at We_n = 29.80, with We_t = 0 and We_t = 44.06 (Multimedia view). After the droplet hits the surface, a liquid film forms as it gradually spreads out towards the maximum spreading radius D_{max}. The droplet then recedes from both ends towards the center, with its height gradually increasing due to the conversion of surface energy into kinetic energy. Once sufficient kinetic energy has accumulated, the droplet will start to bounce off the surface.

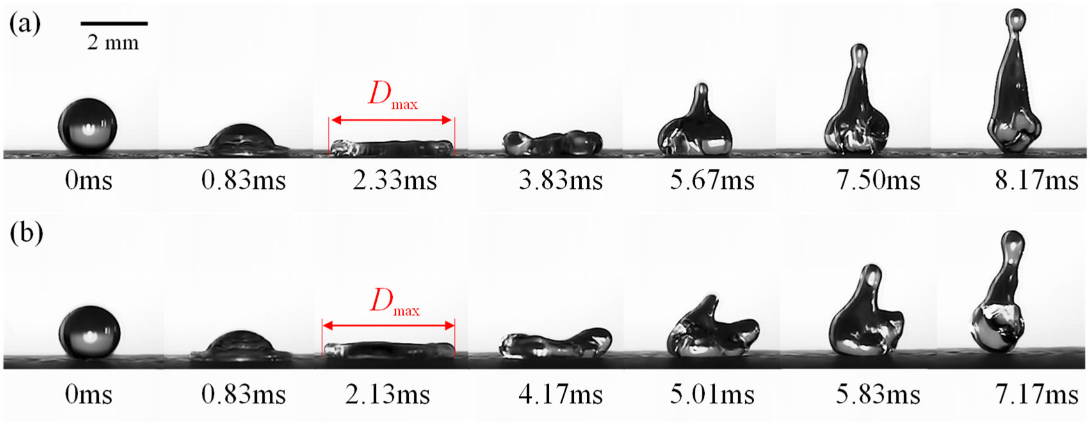

Figure 2. (a) Snapshot of droplet impact on the SHPS for We_n = 29.80 and We_t = 0. (b) Snapshot of droplet impact on the SHPS for We_n = 29.80 and We_t = 44.06. (Multimedia view).

When the surface is stationary, the receding rates of the droplet from both ends are the same (Figure 2(a), t = 3.83 *ms*), resulting in a symmetric bouncing phenomenon. When the surface is in motion, the receding rate on the upstream side is faster than on the downstream side. (Where downstream refers to the side in the direction of surface movement and the upstream side refers to the opposite direction, as shown in Figure 7(a), we will discuss the upstream and downstream in the subsequent sections.) This is due to the influence of surface velocity, causing more kinetic energy to accumulate on the upstream side resulting in a higher height than the downstream side, leading to an "L"-shaped droplet (Figure 2(b), t = 5.01 ~ 5.83 *ms*). As the surface velocity increases, the spreading length of the droplet is stretched longer under the influence of the surface forces, making the "L"-shape more pronounced. Subsequently, the droplet begins to bounce off the surface, compared to the stationary surface, the contact time is reduced from 8.17 *ms* to 7.17 *ms* when the surface is in motion. When the surface is stationary, both ends of the droplet simultaneously leave the surface, while in motion, the downstream side of the droplet will detach from the surface before the upstream side (Figure 2(b), t = 4.17 *ms*). This reduces the portion of the droplet in contact with the surface, leading to a reduction in the contact time [33].

In addition, we conducted statistical analysis of experiments involving different We_t and We_n for contact time, Figure 3(a) shows the normalized contact time τ/τ_0 as a function of We_t under different We_n conditions, where $\tau_0 \approx \sqrt{\left(\frac{\rho D_0^3}{\sigma}\right)}$ is the inertial-capillary time [34]. As seen, the contact time gradually decreases as We_t increases. The difference between the contact times at $We_t = 0$ and $We_t = 116$ is about 30%. However, the influence of different We_n groups on the contact time is relatively weak, these findings are consistent with previous conclusions on moving SHPSs [24,28].

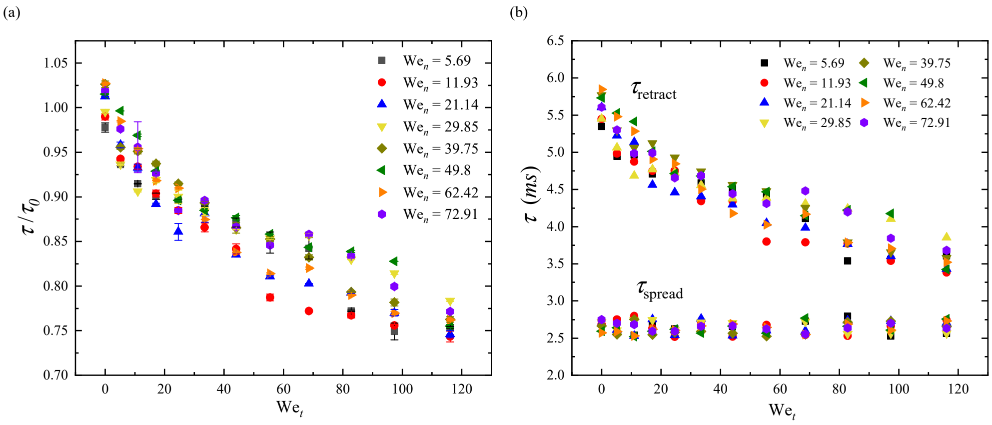

Figure 3. (a) Normalized contact time τ/τ_0 under different We_n groups varies as the change of We_t, where τ_0 is the inertial-capillary time. (b) Spreading time τ_{spread} and retraction time $\tau_{retract}$ varies as the change of We_t.

A. Momentum transfer of droplet on the moving surface.

The bouncing and spreading of droplets are essentially the exchange of kinetic energy and surface energy. When a droplet hits a stationary surface, it bounces vertically along the impact direction, while during surface motion, the rebound direction of the droplet tilts towards the direction of surface motion. Research has shown that there are two theories explaining the cause of this phenomenon. The first theory based on the aerodynamic Leidenfrost effect suggests it is due to the thin layer of air formed between the droplet and the surface [28], while the second theory proposes it is the result of liquid-surface contact forming a viscous boundary layer [30]. We are inclined towards the latter theory. Furthermore, this study is based on the no-slip boundary condition and derives the scaling relationship for the horizontal speed of droplet.

Accordingly, we calculated the center of mass from the shape of droplet in the side view, taking the moment of contact $t = 0$ *ms* as the starting point and the moment of rebound as the end point [Figure 4(a)], by measuring the displacement of the center of mass and the contact time, the averaged horizontal velocity V_a of droplet can be obtained.

Initially, $V_a = 0$, but due to the shear effect of the surface, the momentum increases during the impact process. Considering the total viscous force and combine Newton's second law in the horizontal direction $mdV_a/dt = F(t)$, the average velocity in the horizontal direction can be obtained [30]:

$$V_a = \frac{3\mu V_t}{2\rho D_0^3}\frac{1}{\delta_0}\int_0^t D^2(t)dt \tag{1}$$

where μ is the viscosity of the liquid, δ_0 is the thickness of the boundary layer, t is the contact time of the droplet on the moving surface and $D^2(t)$ represents the contact area of the droplet. In previous studies, $D^2(t)$ is considered to be the square of the maximum spreading length on a stationary surface $D_{max\text{-}s}$. However, the droplet is not circular on a moving surface. It will be stretched along the direction of surface movement, and the maximum spreading of the droplet in that direction is defined as $D_{max\text{-}}$

doi:10.20944/preprints202311.1790.v1

m, as shown in Figure 4(c). While the maximum spreading length in the perpendicular to horizontal direction is evidently smaller than $D_{\text{max-m}}$, and this spreading length is approximately equal to the spreading length $D_{\text{max-s}}$ on a stationary surface have been demonstrated [35]. Based on this, we can deduce:

$$V_a \sim \frac{3\mu V_t}{2\rho D_0^3}\frac{1}{\delta_0}D_{\max-m}D_{\max-s}t \tag{2}$$

With the maximal spreading ratio of the drop $\beta_{\max} = D_{\max}/D_0$, the dimensionless integral mean value of boundary layer thickness $\delta = \delta_0/D_0$, the dimensionless contact time $\tau = V_n t/D_0$, we can derive that:

$$V_a \sim \frac{3\mu V_t}{2\rho D_0 V_n}\frac{1}{\delta}\beta_{\max-m}\beta_{\max-s}\tau \tag{3}$$

On the moving surface, the maximum spreading ratio $\beta_{\text{max-m}} \sim \text{We}_n^{1/4}\text{Ca}^{1/6}$ [28], where the capillary number $\text{Ca}=\mu V_t/\gamma$. (Despite this equation being based on the aerodynamic Leidenfrost effect, our experimental results have shown good agreement with it, the comparative results in Supplementary Material Figure S1.) While on the stationary surface, the maximum spreading ratio $\beta_{\text{max-s}} \sim \text{We}_n^{1/4}(1-\cos\theta)^{-1/2}$ [36].

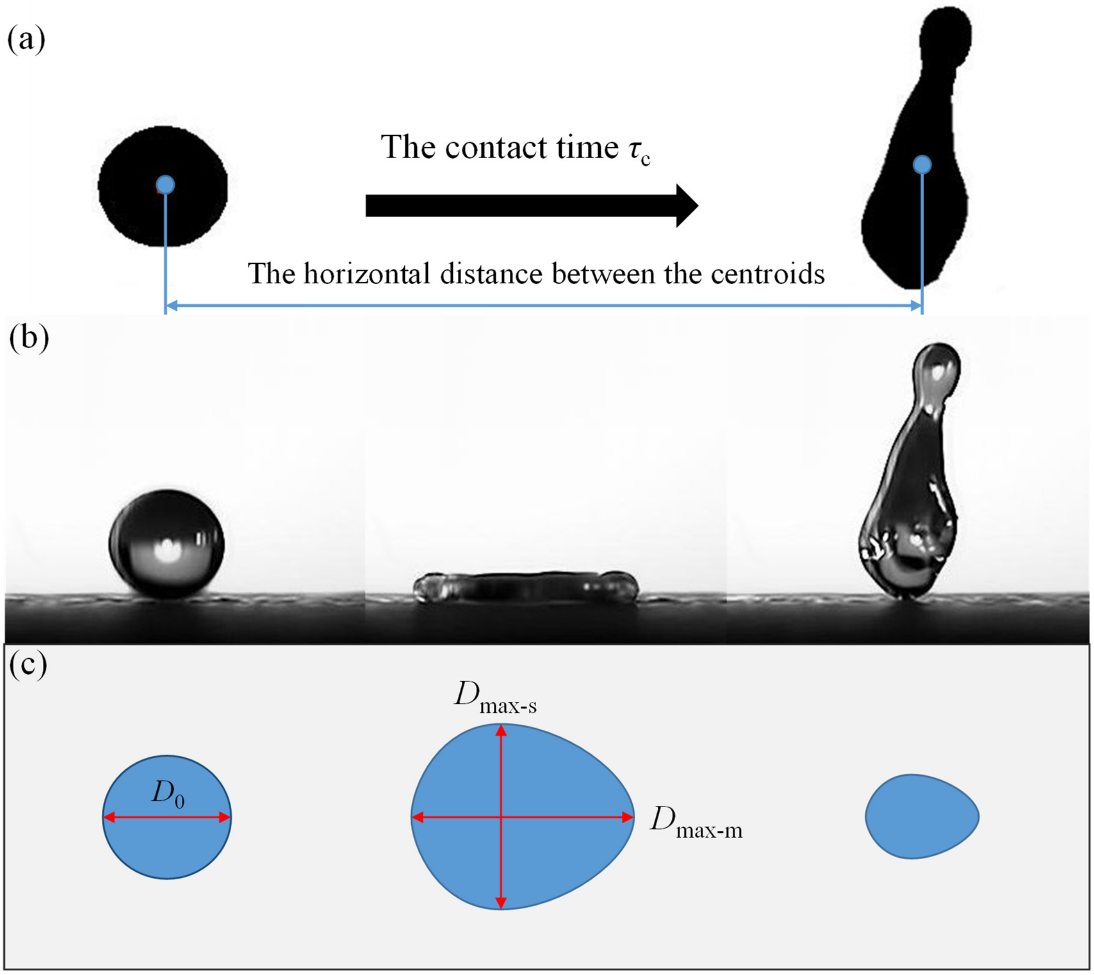

Figure 4. (a) The blue dot represents the centroid of the droplet, from which the droplet velocity V_a is calculated based on the distance moved in the horizontal direction. (b) Side view of the droplet at different time instances. (c) Top view of the droplet at different time instances, where $D_{\text{max-s}}$ and $D_{\text{max-m}}$ denote the maximum spreading lengths of the droplet on stationary and moving surfaces, respectively.

Another aspect that distinguishes our work from previous research is that they considered the contact time τ in Eq. (3) as the contact time on a stationary surface τ_s, while we consider τ as the contact time on a moving surface τ_m. In Figure 3(a), we can clearly observe a significant difference in contact time between τ_s and τ_m. Based on volume conservation, the relationship between these two is given by [37]:

$$\frac{\tau_m}{\tau_s}=\sqrt{\frac{D_{\max-s}}{D_{\max-m}}} \tag{4}$$

The validation of Eq. (3) can be observed in Supplementary Material Figure S2. The contact time on the stationary surface τ_s~$\mathrm{We}_n^{1/2}(1-\cos\theta)^{-1/2}$. By combining Eq. (3) and Eq. (4) with the above scaling relationships, we can deduce:

$$V_a \sim \frac{3}{2\delta}(1-\cos\theta)^{-\frac{5}{4}}\,\mathrm{Re}^{-1}\,\mathrm{We}_n\,\mathrm{Ca}^{\frac{1}{12}}V_t \tag{5}$$

Where the dimensionless Reynolds number is defined as $\mathrm{Re}=\rho V_n D_0/\mu$, Eq. (5) is derived using the contact time τ_m and maximum spreading ratio $\beta_{\text{max-m}}$ on a moving surface. If we were to derive it using the contact time τ_s and maximum spreading ratio $\beta_{\text{max-s}}$ on a stationary surface [30], we can derive:

$$V_a \sim \frac{3}{2\delta}(1-\cos\theta)^{-\frac{3}{2}}\,\mathrm{Re}^{-1}\,\mathrm{We}_n V_t \tag{6}$$

When comparing Eq. (5) and (6), the difference is the additional influence of the capillary number Ca in Eq. (5). This inclusion of Ca enhances the influence of surface motion on the droplet velocity and making it a more accurate representation. The boundary layer thickness and contact angle can be regarded as constant values. Therefore, the Eq. (5) can be expressed as:

$$V_a \sim \mathrm{Re}^{-1}\,\mathrm{We}_n\mathrm{Ca}^{\frac{1}{12}}V_t \tag{7}$$

In Figure 5, we can observe a good consistency between the experimental data and Eq. (6).

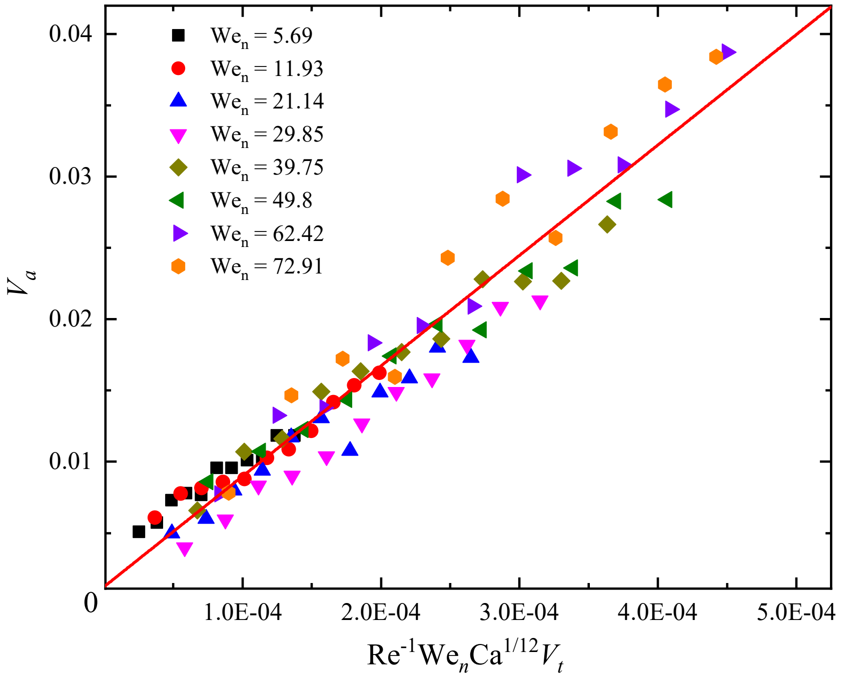

Figure 5. Variation of the V_a as a function of Re, We_n, Ca and V_t, with the solid line representing the best fit of Eq. (6).

As previously mentioned, the conversion of momentum during droplet impact involves the consumption of energy. This implies that the averaged horizontal velocity of the droplet V_a should be lower than the surface velocity V_t. We found that the velocity of the droplet is only about 1% of the surface movement velocity. As a result, we defined the averaged restitution coefficient $\varepsilon_t = V_a/V_t$. Previous research has demonstrated a negative correlation between We_n and ε_t because higher We_n impacts can cause more significant droplet deformation, leading to more energy dissipation during rebound and a decrease in ε_t [38-42]. However, our study on the moving surface revealed an opposing result, we found that ε_t increases with the increase of We_n, as shown in Figure 6(a), and there is no significant change with the increase of We_t, as shown in Figure 6(b), the black line in the box represents the median line, and the point in the middle is the mean value. The upper and lower boundaries of the box represent the upper interquartile and lower interquartile, respectively, while the whiskers represent the extreme values. Firstly, previous studies focused on instantaneous velocity, while this study specifically examines the average velocity throughout the entire impact process. Secondly, a significant factor is that as the droplet impacts a moving surface, with an increase in the Weber number, the spreading length increases. This results in the viscous boundary layer length between the droplet and the surface also increasing, leading to an increase in the force exerted on the droplet in the horizontal direction. Ultimately, this is manifested as an increase in the coefficient of restitution.

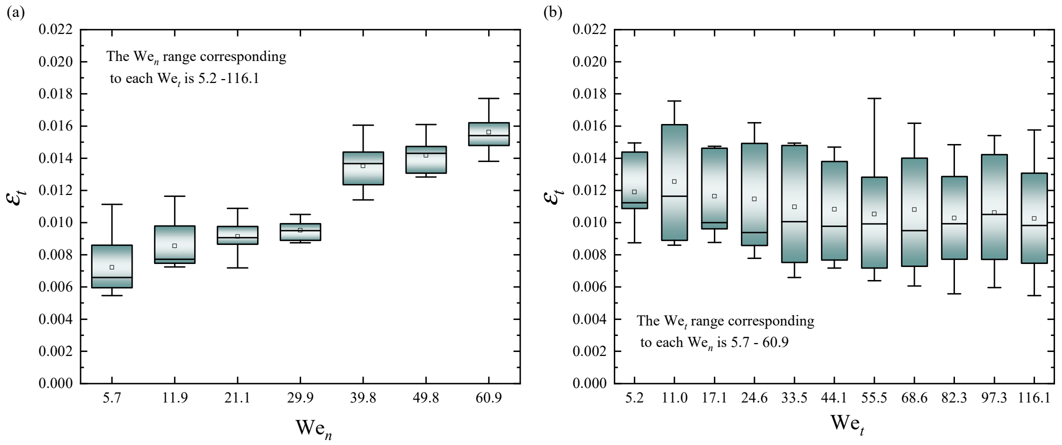

Figure 6. (a) The boxplot of tangential recovery coefficient ε_t with respect to We_n which range corresponding to each We_t is 5.2-116.1. (b) The boxplot of tangential recovery coefficient ε_t with respect to We_t which range corresponding to each We_n is 5.7-60.9.

B. Morphology of droplet on moving surface

We conducted an analysis of changes in droplet behavior from a momentum perspective. In addition, the most significant difference between the stationary and moving surfaces is not only the contact time, but also the asymmetric spreading and receding of the droplet on the upstream and downstream sides.

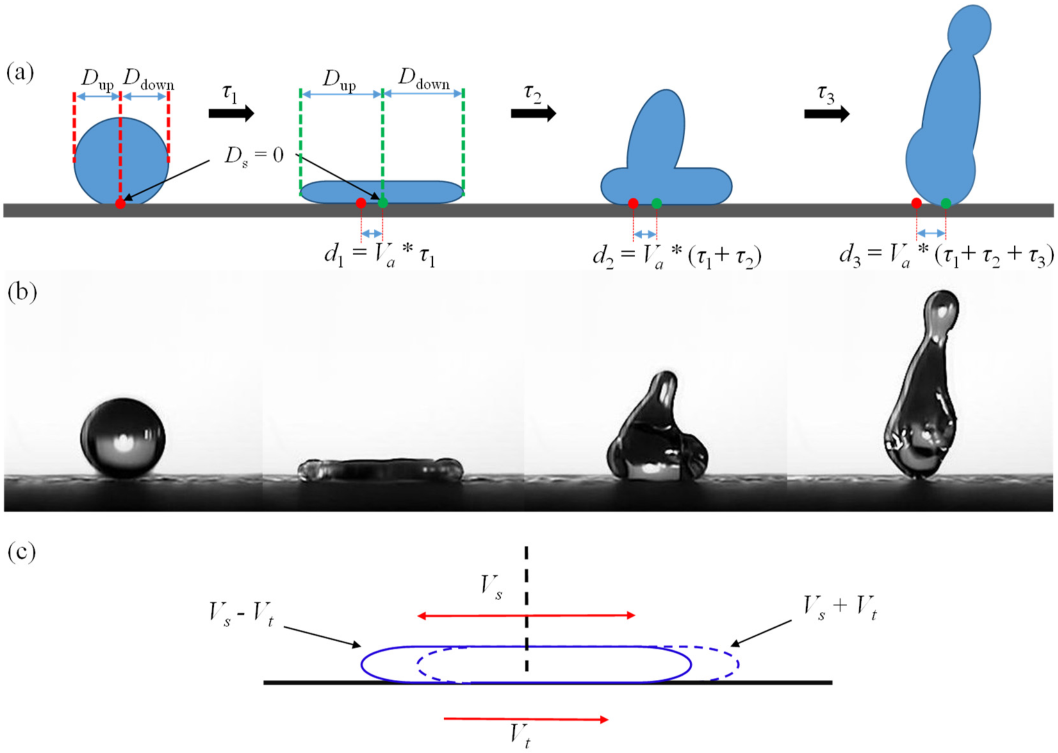

Figure 7. (a) Schematic diagram distinguishing the upstream and downstream spreading of the droplet. The red dot represents the initial center of impact of the droplet, while the green dot indicates the position after moving with velocity V_a. The green dot serves as the reference for defining the boundary between the upstream and downstream regions, where D_s=0. (b) Side view of the droplet at different time instances. (c) Schematic representation of the velocity superposition of V_s and V_t.

Therefore, we divided the droplet into two portions D_{up} and D_{down} based on the impact center point. Initially, the positions of the center points D_s=0 is represented by the red dot [Figure 7(a)]. And it varies at different moments, it moves with the horizontal velocity V_a of the droplet, as indicated by the green point in Figure 7(a). The distance from the point along the moving direction to the edge of the droplet is referred to as D_{up}, and the distance from the point along the opposite direction of motion to the edge of the droplet is referred to as D_{down}. When We_t =0, the spreading length of the droplet on the upstream and downstream sides is symmetrically distributed along D_s=0. However, as We_t increases, the spreading length of the droplet on the upstream side gradually increases, and its spreading time becomes longer, as shown in Figure 8(a) and 8(b), the negative values in Figure 8(a) represent that the droplet is located to the right of the boundary point. In addition, the time of initiating receding on the upstream side is later than that on the downstream side. For different We_t values, the spreading time of the downstream side is around 2 *ms*, and it has almost no effect on the length of spreading. However, the length during the receding phase gradually reduces with the increase of surface speed. In Figure 8(c) and 8(d), with a fixed We_t = 44.06 and different We_n, the spreading length on both the upstream and downstream sides increases with We_n, with the increment being more significant on the downstream side.

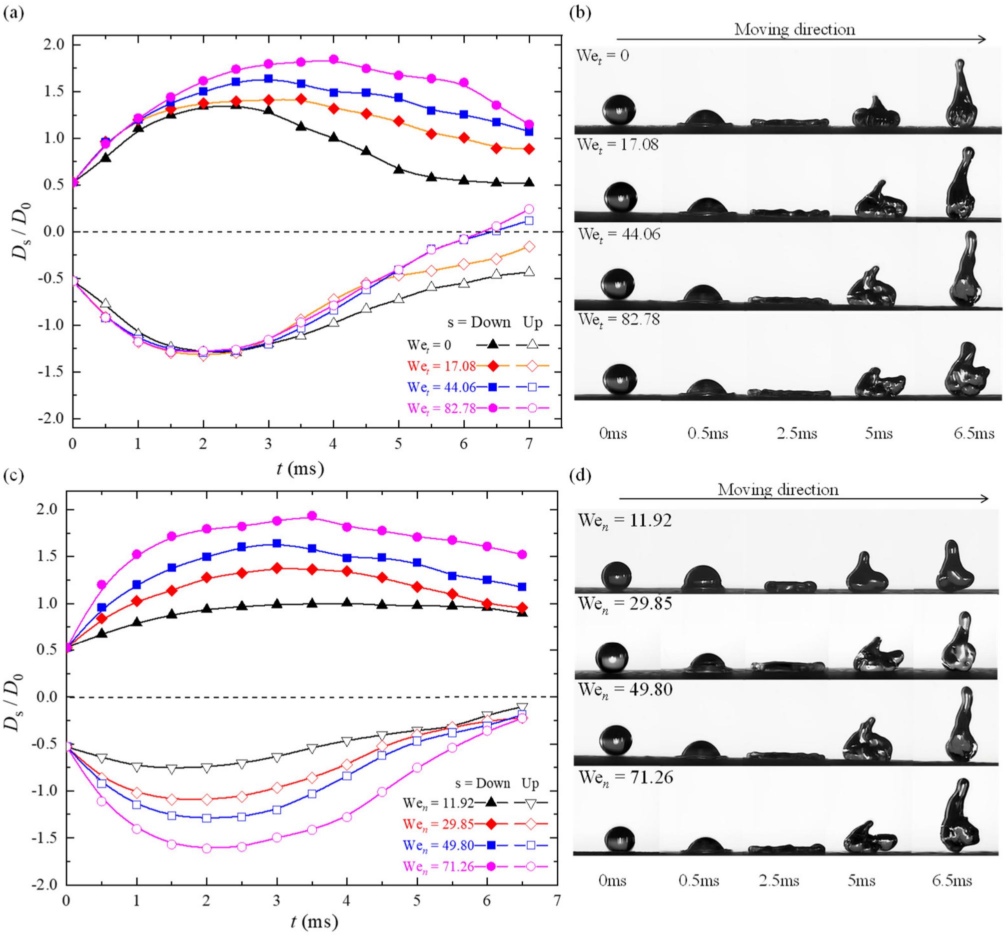

Figure 8. (a) Variation of upstream and downstream spread lengths of the droplet with time for different values of We_t at $We_n = 49.8$, with the center of the droplet at $D_s = 0$ at the beginning of impact used to distinguish between the upstream and downstream regions. (b) Actual deformation of the droplet corresponding to (a). (c) Variation of upstream and downstream spread lengths of the droplet with time for different values of We_n at $We_t = 44.06$. (d) Actual deformation of the droplet corresponding to (c).

Although the increment of spreading length on the upstream side during the receding phase is relatively small compared to that in the spreading phase, it still increases overall. Thus, we postulate that when the droplet reaches its maximum spreading length, the length of the upstream and downstream portions should be a function of the impact velocity V_n and surface velocity V_t. Assuming that the averaged spreading velocity is V_s and the surface velocity is V_t, the averaged velocity of the upstream can be treated as $V_{up} = V_s - V_t$, similarly, the averaged velocity of the downstream is $V_{down} = V_s + V_t$, as shown in Figure 7(c). Taking into account that droplet will also move a certain distance caused by the moving substrate, the maximal spread length ratio of the upstream to downstream can be expressed as:

$$\frac{D_{\text{up}}}{D_{\text{down}}} \sim \frac{(V_s - V_t)\tau_{\text{spread}} - V_a \tau_{\text{spread}}}{(V_s + V_t)\tau_{\text{spread}} + V_a \tau_{\text{spread}}} \tag{8}$$

If the droplet's upstream and downstream are distinguished based on the calculated moving distance of the green dot, then the term $V_a \tau_s$ representing the sliding distance of the droplet in Eq. (7) can be eliminated, the formula can be simplified as:

$$\frac{D_{\mathrm{up}}}{D_{\mathrm{down}}} \sim \frac{V_s - V_t}{V_s + V_t} \tag{9}$$

Obviously, $V_t \sim \alpha \mathrm{We}_t^{1/2}$, and for V_s, it is a function of the maximum spreading length and spreading time, $V_s \sim D_{\max}/\tau_{\mathrm{spread}}$. As can be observed in Figure 3(b), the spreading time τ_{spread} is independent of surface velocity and impact velocity, which is consistent with previous research findings [3,28]. Therefore, we can treat τ_{spread} as a constant, while $D_{\max} \sim D_0 \mathrm{We}_n^{1/4}$, based on these, we can derive the expression for $V_s \sim \beta \mathrm{We}_n^{1/4}$, Substituting these values into Eq. (8) we have:

$$\frac{D_{\mathrm{up}}}{D_{\mathrm{down}}} \sim \frac{\alpha \mathrm{We}_n^{1/4} - \beta \mathrm{We}_t^{1/2}}{\alpha \mathrm{We}_n^{1/4} + \beta \mathrm{We}_t^{1/2}} \tag{10}$$

Where coefficients α and β are related constants, Eq. (10) can be written as Eq. (11):

$$\frac{D_{\mathrm{up}}}{D_{\mathrm{down}}} \sim 1 - \frac{2\mathrm{We}_t^{1/2}}{k\mathrm{We}_n^{1/4} - \mathrm{We}_t^{1/2}} \tag{11}$$

Where coefficients $k=\alpha/\beta$. In Figure 9, we can observe a good consistency between the experimental data and Eq. (11). This scaling relationship has practical applications such as using water to cool rotating machinery, understanding the spreading range of droplet holds significance for such applications [43].

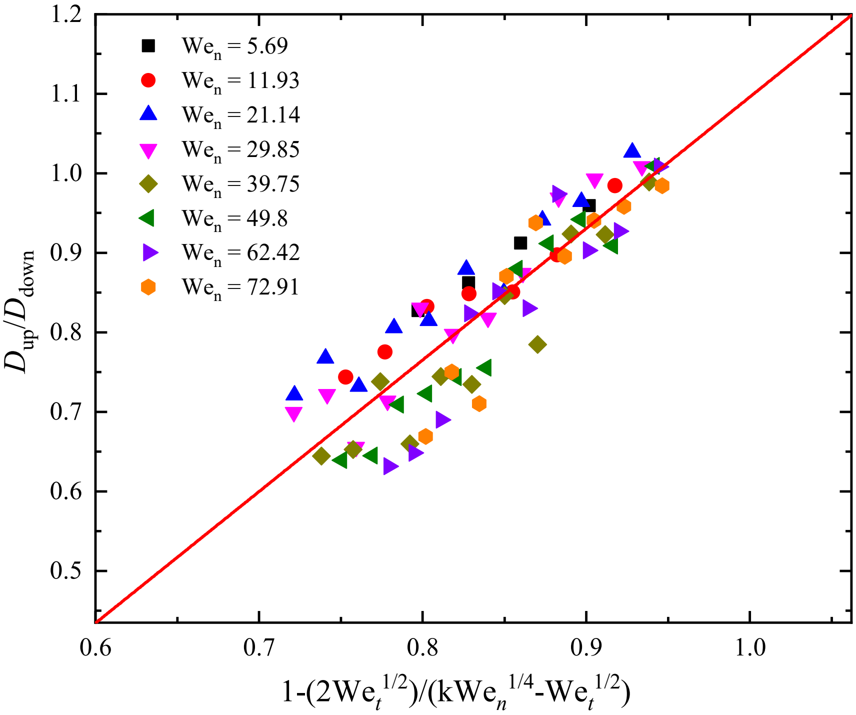

Figure 9. We_t and We_n as functions of the normalized ratio of upstream and downstream spread lengths, the solid line representing the best fit of Eq. (11).

IV. CONCLUSIONS

In this study, experiments have shown that the contact time between water droplets and surfaces is inversely proportional to surface velocity. Our main conclusions are as follows. 1. We have refined the scaling relationship for the horizontal velocity V_a of the droplet. Previous conclusions were derived by approximating the droplet's spreading on a moving surface as a circular shape, and in doing so, the droplet's contact time τ_m was considered equal to τ_s. However, in actually, the droplet elongates in the direction of surface motion, considering it as a circular is inaccurate. And the droplet's contact time on a moving surface τ_m is less than τ_s. These corrections make the scaling relationship more accurate. 2. Furthermore, an investigation into the variation relationship between the droplet's tangential restitution coefficient ε_t and Weber numbers We_n and We_t was conducted. Additionally, we were surprised to discover that the velocity of the droplets was only about 1% of the SHPSs speed, we will focus on exploring ways to improve the exchange rate of droplet momentum in future work. 3. Based on the asymmetry of droplet spreading, a coupling scale relationship between the maximum spreading length ratio of water droplets upstream and downstream was revealed by superimposing the spreading velocity and the surface velocity, which finding can be applied to temperature reduction in moving machinery. These has provided us with new insights into the energy transfer mechanisms of small droplets.

Supplementary Materials: The following supporting information can be downloaded at the website of this paper posted on Preprints.org. Figure S1: The validation of the maximum spreading ratio $\beta_{\text{max-m}}$ on a moving surface. Figure S2: The validation of the contact time τ_m on a moving surface.

Acknowledgments: This work was supported by the National Natural Science Foundation of China (Grant No. 12002212, 11872283) and Shanghai Sailing Program (Grant No. 20YF1432800). The grant is gratefully acknowledged.

Data Availability: The data that support the findings of this study are available within the article and its supplementary material.

References

1. X. Cheng, T.-P. Sun, and L. Gordillo, Annual Review of Fluid Mechanics **54**, 57 (2022).
2. J. De Ruiter, R. Lagraauw, D. Van Den Ende, and F. Mugele, Nature physics **11**, 48 (2015).
3. C. Josserand and S. T. Thoroddsen, Annual review of fluid mechanics **48**, 365 (2016).
4. R. Enright, N. Miljkovic, J. Sprittles, K. Nolan, R. Mitchell, and E. N. Wang, ACS nano **8**, 10352 (2014).
5. F. Liu, G. Ghigliotti, J. J. Feng, and C.-H. Chen, Journal of Fluid mechanics **752**, 39 (2014).
6. X. Liu, P. Cheng, and X. Quan, International Journal of Heat and Mass Transfer **73**, 195 (2014).
7. X. Han, J. Li, X. Tang, W. Li, H. Zhao, L. Yang, and L. Wang, Small **18**, 2200277 (2022).
8. X. Yu, Y. Zhang, R. Hu, and X. Luo, Nano Energy **81**, 105647 (2021).
9. A. R. Esmaeili, N. Mir, and R. Mohammadi, Langmuir **37**, 841 (2021).
10. H. Liu, C. Si, C. Cai, C. Zhao, and H. Yin, Chemical Engineering Science **229**, 116106 (2021).
11. V. Fink, X. Cai, A. Stroh, R. Bernard, J. Kriegseis, B. Frohnapfel, H. Marschall, and M. Wörner, International Journal of Heat and Fluid Flow **70**, 271 (2018).
12. K. Okumura, F. Chevy, D. Richard, D. Quéré, and C. Clanet, Europhysics Letters **62**, 237 (2003).
13. Y. Guo, Y. Lian, and M. Sussman, Physics of Fluids **28**, 073303 (2016).
14. C. S. Stevens, A. Latka, and S. R. Nagel, Physical Review E **89**, 063006 (2014).
15. T.-S. Zen, F.-C. Chou, and J.-L. Ma, International communications in heat and mass transfer **37**, 1025 (2010).
16. W. Yu, D. Zhu, W. Wang, Z. Yu, S. Chen, and J. Zhao, Applied Physics Letters **121**, 061602 (2022).
17. C. Clanet, C. Béguin, D. Richard, and D. Quéré, Journal of Fluid Mechanics **517**, 199 (2004).
18. M. J. Kreder, J. Alvarenga, P. Kim, and J. Aizenberg, Nature Reviews Materials **1**, 1 (2016).
19. S. Ren, S. Wang, Z. Dong, J. Chen, and L. Li, Colloids and Surfaces A: Physicochemical and Engineering Aspects **626**, 127056 (2021).
20. J. C. Bird, R. Dhiman, H.-M. Kwon, and K. K. Varanasi, Nature **503**, 385 (2013).
21. Y. Liu, G. Whyman, E. Bormashenko, C. Hao, and Z. Wang, Applied Physics Letters **107**, 051604 (2015).
22. J. Hou, J. Gong, X. Wu, and Q. Huang, International Journal of Heat and Mass Transfer **183**, 122044 (2022).
23. N. Reis, C. Ainsley, and B. Derby, Journal of Applied Physics **97**, 094903 (2005).
24. X. Zhang, Z. Zhu, C. Zhang, and C. Yang, Applied Physics Letters **117**, 151602 (2020).
25. R. Tao *et al.*, Research **6**, 0023 (2023).
26. F. Chu, S. Li, Z. Hu, and X. Wu, Applied Physics Letters **122** (2023).

27. A. Gauthier, J. C. Bird, C. Clanet, and D. Quéré, Physical Review Fluids **1**, 084002 (2016).
28. H. Zhan, C. Lu, C. Liu, Z. Wang, C. Lv, and Y. Liu, Physical Review Letters **126**, 234503 (2021).
29. P. García-Geijo, G. Riboux, and J. M. Gordillo, Journal of Fluid Mechanics **897**, A12 (2020).
30. M. Wang *et al.*, Iscience **26** (2023).
31. Y. Shu, F. Chu, Z. Hu, J. Gao, X. Wu, Z. Dong, and Y. Feng, ACS Applied Materials & Interfaces **14**, 57340 (2022).
32. A. M. Moqaddam, S. S. Chikatamarla, and I. V. Karlin, Journal of Fluid Mechanics **824**, 866 (2017).
33. S. Moghtadernejad, M. Jadidi, J. Hanson, and Z. Johnson, Physics of Fluids **34**, 062104 (2022).
34. D. Richard, C. Clanet, and D. Quéré, Nature **417**, 811 (2002).
35. H. Almohammadi and A. Amirfazli, Langmuir **33**, 5957 (2017).
36. S.-R. Gao, B.-J. Wei, J.-X. Jin, J.-S. Ye, Y.-F. Wang, S.-F. Zheng, Y.-R. Yang, and X.-D. Wang, Physics of Fluids **34** (2022).
37. X. Zhang, Z. Zhu, C. Zhang, and C. Yang, Applied Physics Letters **117** (2020).
38. A. I. Aria and M. Gharib, Langmuir **30**, 6780 (2014).
39. V. Bertola, International journal of heat and mass transfer **52**, 1786 (2009).
40. A.-L. Biance, F. Chevy, C. Clanet, G. Lagubeau, and D. Quéré, Journal of Fluid Mechanics **554**, 47 (2006).
41. L. Chen, Z. Xiao, P. C. Chan, Y.-K. Lee, and Z. Li, Applied surface science **257**, 8857 (2011).
42. L. Qian, B. Huo, Z. Chen, E. Li, and H. Ding, International Journal of Multiphase Flow **165**, 104454 (2023).
43. A. L. Yarin, Annu. Rev. Fluid Mech. **38**, 159 (2006).